ELSEVIER

Contents lists available at ScienceDirect

Journal of Colloid and Interface Science

journal homepage: www.elsevier.com/locate/jcis



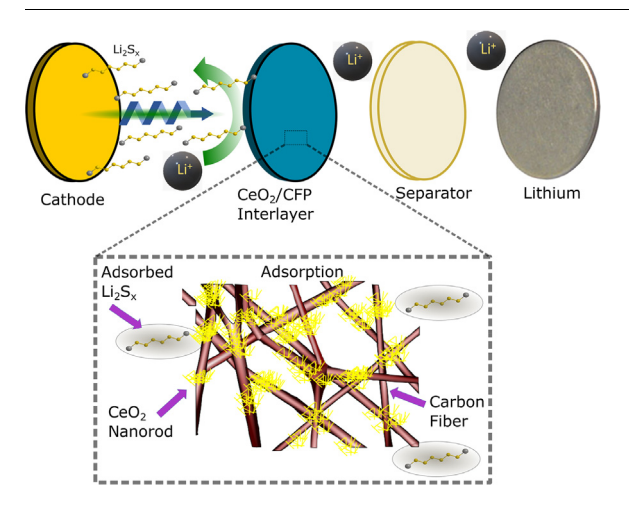
Cerium oxide nanorods anchored on carbon nanofibers derived from cellulose paper as effective interlayer for lithium sulfur battery



Sakibul Azam, Zhen Wei, Ruigang Wang*

Department of Metallurgical and Materials Engineering, The University of Alabama, Tuscaloosa, AL 35487, United States

G R A P H I C A L A B S T R A C T



ARTICLE INFO

Article history: Received 23 October 2021 Revised 16 January 2022 Accepted 25 January 2022 Available online 29 January 2022

Keywords: Lithium sulfur batteries Lithium polysulfides Shuttle effect Interlayer Cerium oxide

ABSTRACT

Investigation of sluggish redox kinetics and polysulfide shuttling is crucial to design advanced lithium sulfur battery. Cerium oxide (CeO₂) has remarkable polysulfide adsorption capability and has been recently investigated in lithium sulfur battery application. With the goal of bridging towards commercialization of lithium sulfur battery, cellulose paper derived carbon fiber decorated with CeO₂ nanorods using hydrothermal method has been fabricated and used as interlayer material for lithium sulfur battery. In this novel design, the carbon fiber provides physical confinement with its 3-D interconnected conductive structure and CeO₂ adsorbs lithium polysulfides chemically to reduce shuttle effect to achieve long lifetime and high capacity for lithium sulfur battery. With a sulfur content of 2 mg, a high capacity of 1177 mAhg⁻¹ was achieved at 0.2C with an excellent stability of only 0.11% capacity decay per cycle over 300 cycles. The improved performance is attributed to the binding of lithium polysulfides by CeO₂ and the blocking of polysulfides physically by the compact conducting carbon fiber.

© 2022 Elsevier Inc. All rights reserved.

1. Introduction

Energy consumption is a major global issue of the 21st century with the rapid development of the fast-paced society. To fully utilize the environmentally benign and renewable energy sources like

^{*} Corresponding author.

E-mail address: rwang@eng.ua.edu (R. Wang).

solar power, wind power, and geothermal energy etc., there is an urgent need of energy storage devices due to their intermittent nature. For more than a few decades, rechargeable Li ion batteries (LIBs) have been studied and/or used prevalently in consumer electronics applications, portable electronics, electric vehicles, and uninterrupted power supply devices. But the current LIB technology still lacks the performance because of low energy density, that comes at a high cost. Lithium sulfur (Li-S) battery is a promising candidate to replace conventional LIBs due to its high theoretical capacity (1675 mAhg⁻¹) which is about 3-5 times higher than that of LIBs, reasonable operating voltage of 2 V, high theoretical energy density (2600 Whkg⁻¹), less toxicity and cost effectiveness. Since sulfur is an earth abundant material (the 17th richest element), the electrode material cost per kilowatt hour is much cheaper than the other high energy density battery electrode materials [1]. At present. LIBs have low specific capacity of less than 300 mAhg⁻¹ and the Li insertion mechanism in the popular cathode materials like LiFePO₄, LiCoO₂ restricts the ability of improving the energy density of the cells [2-9]. It also requires the use of transition metal phosphates or oxides to preserve the crystallinity. On the other hand, Li-S batteries use two lithium atoms to preserve the crystalline structure without the need of any additional atom. This two-electron transfer mechanism during cycling, and the high theoretical energy density/specific capacity make Li-S battery a viable choice to replace Li ion technology in energy storage devices. Despite being a promising alternative to Li ion battery due to the high theoretical energy density and abundance of sulfur, Li-S battery is yet to be commercialized because of some critical technical issues and there is still significant room for improvement for stable Li-S battery with long cycle life. The major problems associated with the Li-S batteries are (i) the insulating nature of sulfur $(5 \times 10^{-30} \, \text{S cm}^{-1} \, \text{at room temperature})$ and its reaction products (Li₂S₂/Li₂S) [10-12], (ii) the notorious "shuttling effect" of dissolved higher order lithium polysulfides in the liquid electrolyte [13–15], (iii) volume change (\sim 80%) of cathode active material during cycling [16,17], (iv) dendrite formation in lithium anode causing morphological change and short circuiting of the battery [18] and (v) electrochemical performance degradation due to N₂ and N₂O gases [19].

To meet the criteria towards commercialization of Li-S batteries, researchers have focused on developing novel porous carbon materials for cathode and various encapsulation strategies to block polysulfide shuttling [20-24]. Much emphasis was also put on developing interlayer materials to trap polysulfides chemically and physically to improve the lifetime of the battery. A membrane between the cathode and the separator known as "interlayer" was previously demonstrated by Manthiram's group [25,26]. The electrolyte permeable microporous interlayer can act as a viceelectrode expanding the area for extra reaction sites and work as an extra layer to adsorb or immobilize the polysulfides. A conductive interlayer can promote fast electron transfer from the cathode to the interlayer improving redox reaction kinetics. It also provides protection from Li anode corrosion since it collects the deposited lithium discharge products on its surface which can be reused in the cathode [27]. However, using the interlayer between the separator and the anode would be inappropriate, since, it won't facilitate the reuse of the sulfur discharge products in the cathode. Fan et al. used carbonized cellulose paper as an effective interlayer to suppress polysulfide shuttling [28]. It was demonstrated that the interlayer can improve the conductivity as well as provide valid physical confinement to inhibit polysulfide shuttling. In addition, Huang et al. used carbonized bacterial cellulose as an interlayer in the Li-S battery to prevent the aggregation of sulfur in the cathode [29]. Cui et al. reported interlayer design with a two dimensional layered structure of metal disulfides to encapsulate polysulfides by bonding with Li_2S_n/Li_2S and forming Li-S bond [30].

Various porous high-surface-area carbonaceous nanomaterials can physically trap the lithium polysulfides (Li_2S_n : 4 < n < 8) and also work as current collector owing to their outstanding conductivity. However, although these carbon-based materials show excellent Li₂S_n trapping capability in laboratory test cells, the fabrication method of these proposed interlayers involves complex process and is not a viable option for large scale synthesis of interlayer membranes. Thus, a facile and simple synthesis route to fabricate porous carbon-based interlayer material is a compelling topic of research. Cellulose is an earth abundant organic compound or biomaterial that contains structural components of cell membrane/walls or texture. The source of cellulose is very common due to the biomass feedstock derived from agriculture crops or their wastes. Cellulose contains a large number of carbon bonds in its structure, and its abundance and low cost make it a popular choice as carbon source. Cellulose derived carbon structure has good mechanical hardness, excellent electrical conductivity owing to the interconnected fiber network providing fast electron transport pathway, and large surface area for electrolyte contact [31]. Therefore, pyrolyzed cellulose can be used as another carbonbased effective interlayer for Li-S battery as Fan et al. demonstrated previously [28]. However, the porous carbon nanofibers in cellulose can only physically entrap the lithium polysulfides, providing little to no adsorption synergy towards chemically binding the polysulfides and avoiding shuttling. As a result, the assembled battery suffered from rapid capacity decay at 0.2C lasting for only 130 cycles [28].

The Li-S batteries using CeO₂ as catalytic material were reported previously. Particularly, modifying nano-CeO2 on fiber or carbon nanotube has been reported for lithium-sulfur batteries [32,33]. Lu et al. used solvothermal technique to prepare CeO₂ decorated with carbon nanotube webbed structure as cathode host material [33]. Shen et al. prepared a composite of Ketjen Black decorated with homogeneously distributed CeO₂ nanodots to use it as a sulfur host material for Li-S battery [34]. Similar approach was taken by Jin et al. where they implanted CeO₂ nanocrystals inside the porous nitrogen doped carbon nanospheres [35]. The micropores filled with CeO₂ can help entrap the polysulfides for improved Li-S battery performance. Zhang et al. combined spray-drying and hydrothermal process to prepare CeO₂/RGO nanocomposite where RGO works as the conductive support and CeO₂ as polysulfide immobilizer [36]. However, these reported systems did not use freestanding structure as a conductive support to grow CeO₂. Moreover, the decoration of CeO₂ involves complex processing steps including electrospinning [32], solvothermal reaction [33], wet impregnation [34], spray drying and hydrothermal [36] etc. On the contrary, this work is based on scalable, cost-effective and easy fabrication of freestanding carbon fiber derived from commercially available cellulose paper using one step tube furnace carbonization and one pot hydrothermal synthesis of CeO2 nanorods on carbon fiber. Since an additional layer in the form of interlayer adds extra weight to the battery architecture, it is necessary to make a weight efficient interlayer design. The binders, conductive additives and current collectors add unnecessary weight into the interlayer. However, the freestanding interlayer eliminates the use of the binder, conductive additive and current collectors making it an efficient design and increases the sulfur weight ratio.

Previously, our group investigated hydrothermally grown CeO₂ nanorods on carbon cloth as an effective cathode host material for Li-S battery [37]. The surface oxygen functional group of CeO₂ can trap lithium polysulfides by binding with polysulfide anions. Moreover, the reaction of polysulfides with CeO₂ generates *in situ* thiosulfate ([S₂O₃]²⁻) and polythionate ([SO₃S₂SO₃]²⁻) species which provides catalytic effect towards the conversion of polysulfides. The as-prepared cathode host results in excellent battery rate performance. Since we have already done electrode modification using

CeO₂ nanorods, our focus in this work is to innovate alternate and effective approach by developing interlayer material, which is another crucial part nowadays in lithium sulfur battery research. This interlayer can suppress the polysulfide shuttling outside the cathode zone and can also work as conductive current collector to improve the battery reaction kinetics. Although, growing CeO₂ on carbon cloth substrate can be effective as cathode host, carbon cloth with large pores where polysulfides can diffuse through, cannot provide effective physical entrapment towards polysulfides shuttling when used as interlayer material. Inspired by this, in this study, a low cost and easy synthesis method was developed to prepare carbonized cellulose paper as the carbon substrate, which was decorated with hydrothermally grown CeO₂ nanorods used as interlayer material in Li-S battery.

Herein, a novel method is proposed to develop interlayer materials in Li-S battery using a commercial filter paper derived mesoporous carbon fiber structure, which is decorated by CeO₂ nanorods anchored on its 3D framework structure. Instead of using the CeO₂/CFP (carbonized filter paper) membrane as cathode, using this as interlayer acts as the barrier outside the cathode to suppress the polysulfide shuttling and prevent deposition of Li₂S discharge products on Li metal anode. The polysulfides are trapped and deposited on this interlayer instead. It reduces the overall cell impedance as well due to high electrical conductivity of the membrane providing fast electron transfer from the cathode to the interlayer. A facile one step pyrolysis using tube furnace was adopted to obtain the carbon nanofibers by pyrolyzing commercial filter paper. Further, one step hydrothermal method was used to decorate the carbon nanofibers with CeO2 nanorods. The carbon nanofibers provide conductive 3D framework structure and physical entrapment sites of lithium polysulfides. The CeO₂ nanorods anchored on the carbon nanofibers work as adsorption synergistic support to chemically bind the lithium polysulfides and prevent further shuttling as shown in Fig. 1.

2. Experimental

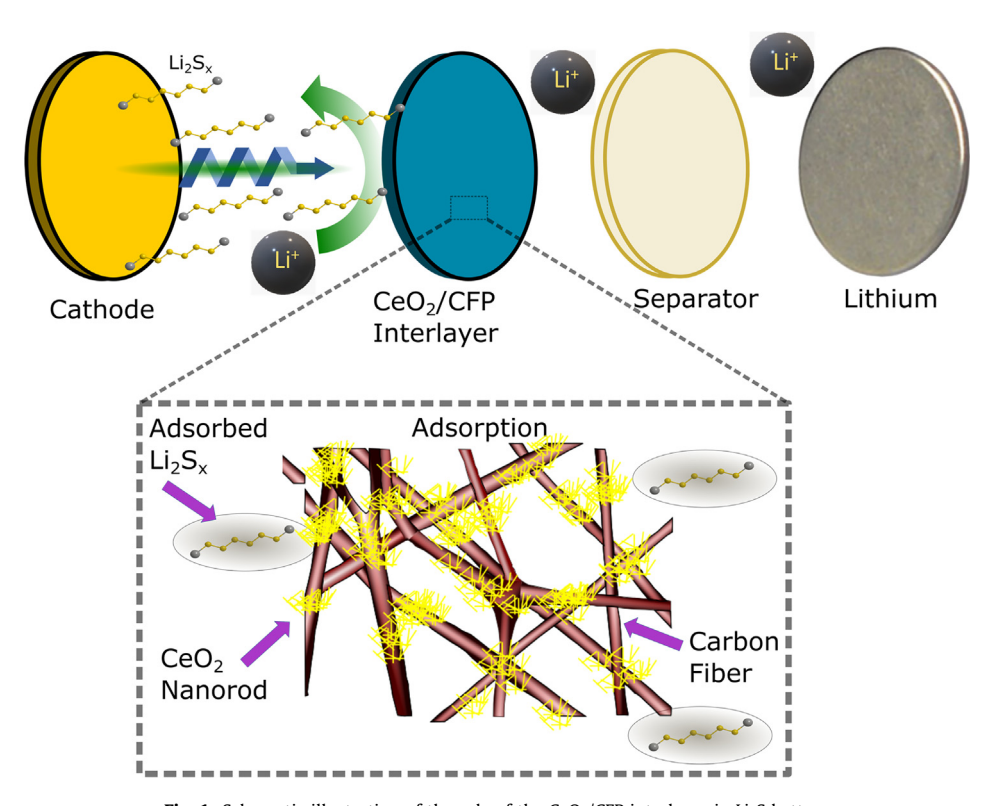
2.1. CeO₂/CFP interlayer preparation

The cerium oxide decorated carbonized filter paper (CeO₂/CFP) interlayer was prepared in a two-step method. Firstly, one piece of commercial filter paper (Whatman Inc.) was carbonized in tube furnace under Ar flow at 800 °C for 2 h. The carbonized filter paper consists of carbon nanofibers which will be used as the substrate in CeO₂ hydrothermal synthesis process. Then, the as-obtained carbon fiber film was put at the bottom of a Teflon lined stainless steel autoclave. Then, 88 mL of 0.1 M cerium nitrate hexahydrate (Ce (NO₃)₃·6H₂O) was mixed with 8 mL of 6.0 M sodium hydroxide (NaOH) in deionized water (DI water) and magnetically stirred for 30 s. The mixture was poured in the autoclave with the carbon fiber film and was hydrothermally treated at 90 °C for 48 h. After the hydrothermal treatment, the as-obtained CeO2 grown on carbon fiber film was obtained, namely CeO₂/CFP. Then it was washed with DI water and ethanol several times and further dried in a vacuum oven at 80 °C overnight. The film was then cut into 15 mm diameter sized circular film and used in Li-S battery.

The amount of CeO_2 was calculated by weighting the CFP before and after hydrothermal treatment. The mass of the CFP with 38 mm diameter was recorded as 23 mg. After hydrothermal and drying, the mass of the CeO_2 /CFP film was recorded as 26.2 mg. So, for the area of 11.34 cm², the amount of CeO_2 was roughly 3.2 mg. As we used 1.5 cm² CeO_2 /CFP interlayer, the amount of CeO_2 per interlayer is approximately 0.42 mg. So, the amount of CeO_2 in the CFP matrix is approximately 12.14% per interlayer.

2.2. Cell assembly

All cells were assembled using CR2032 coin cell from MTI corporation. Stainless steel spacers with 1.5 cm² areal size were used as current collectors. For separators, Celgard 2500 polypropylene



 $\textbf{Fig. 1.} \ \ \textbf{Schematic illustration of the role of the } \ \textbf{CeO}_2/\textbf{CFP interlayer in Li-S battery}.$

with porosity of 55% and pore size distribution of 0.064 was used. Lithium foils with 1.5 cm² circular disks were used as anode. The assembly processes were conducted in an argon filled glovebox (VTI Vacuum Technology Inc.) with oxygen and water contents less than 0.1 ppm. After assembling the cell by hand, it was crimped to tightly seal the cell with a Gelon hydraulic crimper.

The blank electrolyte used in Li-S battery was prepared by making a solution of lithium bis(tri-fluoromethanesulfonyl)imide (LiTFSI) (1.0 M) in 1, 2-dimethoxyethane (DME) and 1, 3-dioxolane (DOL) (1:1 by volume ratio) containing lithium nitrate (LiNO $_3$) (1 wt%). The lithium polysulfide (Li $_2$ S $_6$) catholyte was prepared by chemically reacting sublimed sulfur and lithium sulfide (Li $_2$ S) in the as-prepared blank electrolyte to form 0.5 M Li $_2$ S $_6$ solution. The solution was stirred at 60 °C inside the Ar glovebox for 12 h to obtain dark red lithium polysulfide catholyte.

The battery using CeO₂/CFP as interlayers was assembled by putting the interlayer between the carbon cloth and the separator. The carbon cloth cathode host was first impregnated with 20 µL lithium polysulfide (Li_2S_6) catholyte to obtain ~ 2 mg S loading (1.33 mg/cm²) and used as the positive electrode. After uniformly distributing the catholyte, the DOL/DME solvent was evaporated after a while. Then the as-prepared interlayer film was placed in between the cathode and the separator. The separator was impregnated with 20 µL of blank electrolyte. The amount of electrolyte has a great influence on the performance (i.e., energy density and sulfur utilization) of Li-S battery. Although, commercial Li-S batteries aim for electrolyte to sulfur (E/S) ratio of 4:1 or 3:1, where ether based electrolytes are considered as 10 mg μ L⁻¹, most of the practical Li-S battery publications use E/S ratio of greater than 7:1 [38]. The E/S ratio here is 10:1, which is higher than commercial Li-S battery but lower than many other reported literatures. Finally, the cell was assembled using a hydraulic crimping machine. The diameter of the circular cathode, interlayer and the lithium foil were 15 mm (area $\sim 1.5 \text{ cm}^2$) for all the batteries and the diameter of the separators were 19 mm.

2.3. Electrochemical measurements

The battery cycling test was done in Neware battery testing system. The galvanostatic charge–discharge was conducted at 0.1C, 0.2C, 0.5C and 1C within the voltage range of 1.7 V- 2.8 V. The specific capacity of the battery was calculated according to the mass of the sulfur in the cell with current density of 1C = 1675 m A g $^{-1}$ of S. The Cyclic Voltammetry (CV) and Electrochemical Impedance Spectroscopy (EIS) were conducted using the Gamry instrument Interface-1000 potentiostat/galvanostat/ZRO.

2.4. Materials characterization

Scanning electron microscopy (SEM) images were taken using Thermo Scientific APREO FE-SEM. The accelerated voltage used ranged from 1 kV to 30 kV and the beam current ranges from 13 pA - 40 nA. The low beam current condition was chosen to avoid the charging of the samples. The Energy Dispersive X-ray Spectroscopy (EDS) was done in the same instrument equipped with an EDS characterization system provided by EDAX. The user interface software APEX-EDS was used for elemental mapping analysis and data processing. X-ray photoelectron spectroscopy (XPS) of the as-prepared samples was performed on a VersaProbe 5000 spectrometer with monochromatic Al K α (h ν = 1486.6 eV) radiation at a working pressure of less than 8×10^{-10} Torr. The effect of the specimen charging was corrected by the reference of the carbon peak C 1 s (284.8 eV). The Brunauer-Emmett-Teller (BET) surface area measurement was measured by single point adsorptiondesorption at liquid nitrogen temperature of 77 K using Micromeritics AutoChem II 2920 chemisorption analyzer. The

XRD analysis was taken using a Philips X'Pert MPD X-ray diffractometer with Cu K α radiation (λ = 1.5405 Å) operating at 45 kV and 40 mA. The X-ray data was taken from 10 $^{\circ}$ to 80 $^{\circ}$ of the 2 θ angle with a step size of 0.5°/min and this X-ray instrument is equipped with a goniometer that supports the angular movement. The recorded patterns were analyzed using JADE software to determine peak positions, lattice constant, and average crystalline sizes by use of Scherrer's formula. The Transmission Electron Microscopy (TEM) images were taken using FEI Tecnai F-20. The Raman spectra were taken using Horiba Labram HR 800 Raman spectrometer using 532 nm laser.

3. Results and discussion

3.1. Material fabrication and morphology

The procedure of synthesizing the CeO₂/CFP interlayer is given in Fig. 2. A clean cellulose-based filter paper (Whatman Inc.) was put in a temperature-controlled tube furnace under argon atmosphere with a mass flow controller (200 mL/min) to pyrolyze at 800 °C for two hours with a heating rate of 4°C/min to obtain carbon nanofibers. During pyrolysis, the cellulose fibers decomposed into carbon and lost hydrogen and oxygen. This loss of oxygen and hydrogen is evident from the size reduction of the cellulosebased filter paper from 55 mm diameter and 150 µm thickness to 34.5 mm diameter and 50 μm thickness. The size comparison of the filter paper before and after pyrolysis is given in Fig. 3a. Fig. 3b depicts the SEM image of the morphology and size for the as-prepared carbon fibers derived from cellulose. The diameter of the individual carbon fibers ranges from a few hundred nanometers to $10 \, \mu m$ and the cross-linked morphology of the carbon fibers is maintained like the cellulose fibers after pyrolysis. The filter paper was grinded and turned into powder for BET surface area measurement and 70 mg of samples were loaded in a quartz Utube to conduct the experiment. The surface area was recorded as 172 m²/g. This conductive carbon fiber film was then used as the substrate and anchoring structure to grow CeO2 using hydrothermal synthesis.

To decorate the carbon nanofiber film with CeO_2 nanorods, firstly, the film was put in a Teflon lined stainless steel autoclave. Then the aqueous mixture of cerium nitrate hexahydrate salt (0.1 M $Ce(NO_3)_3$ - GH_2O) and sodium hydroxide (6.0 M NaOH) was slowly poured into the autoclave. The autoclave was then sealed and put in an electric oven for hydrothermal reaction of CeO_2 nanorods under the temperature of $90\,^{\circ}C$ for 48 h. After completion of the hydrothermal synthesis, the carbon fiber film was washed with DI water ($500\,$ mL) and ethanol ($50\,$ mL) several times and dried in a vacuum oven at $60\,^{\circ}C$ for $12\,$ h. This sample was named as $CeO_2/carbonized$ filter paper (CeO_2/CFP) interlayer.

The morphological characterization of the as-prepared CeO₂/ CFP interlayer is also given in Fig. 3. The SEM image in Fig. 3c shows that CeO2 nanorods powders were homogenously distributed in the carbon fiber 3D structure and on the carbon fibers. The higher magnification SEM image of Fig. 3d shows a fiber decorated with CeO2 nanorods. The CeO2 nanorods created a strong contact with the carbon fibers and anchored well on the fiber surface. So, it is evident that, during the growth of CeO₂ nanorods, the carbon fiber 3D structure acted as a supporting scaffold for the nucleation growth of CeO₂ nanorods. In this kind of interlayer material, the highly conductive carbon fiber network provides fast charge transfer network. The pores in the carbon fiber network provide efficient ion diffusion pathway and space for possible volume change during the battery cycling. The CeO₂ nanorods anchored on the carbon fibers can suppress polysulfides shuttling since they show strong interaction and have high bonding affinity

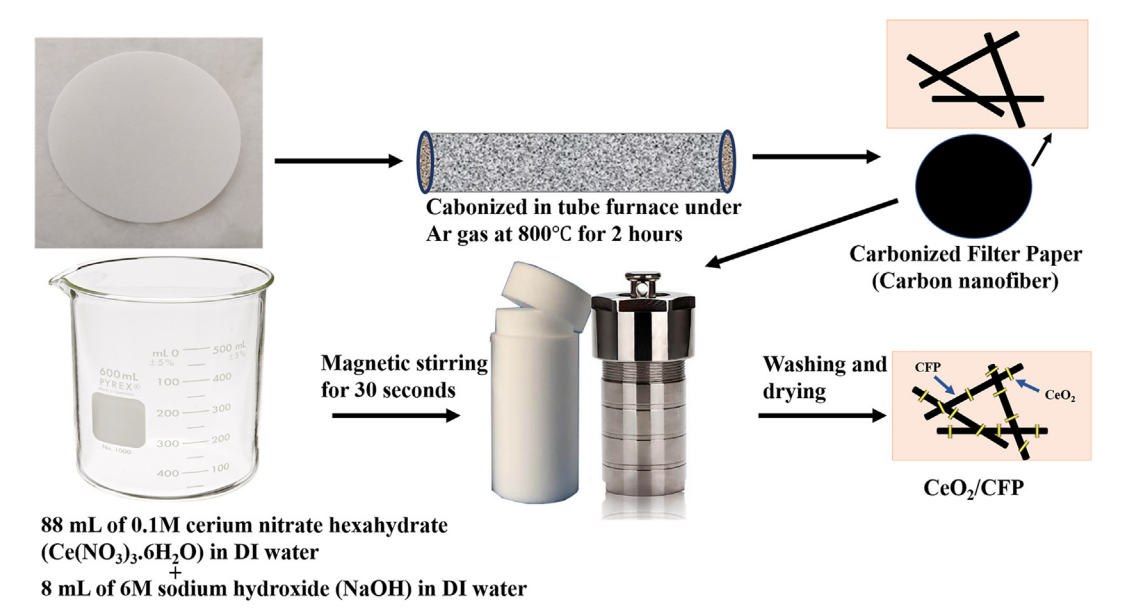


Fig. 2. Schematic illustration of the preparation of the CFP and CeO₂/CFP interlayer.

with the lithium polysulfides via both physical confinement and chemical binding. To show the rod like morphology of CeO_2 , the CeO_2 powders were collected after hydrothermal treatment. The powders were washed with DI water and ethanol several times, and dried at $60\,^{\circ}C$ for 12 h. The as obtained pieces were grounded using mortar to obtain CeO_2 nanorods powder for TEM imaging. The rod like CeO_2 are shown in the TEM images of Fig. 3 (e-f) at different magnifications with diameters ranging from 5 to 10 nm and length $50-150\,$ nm.

Fig. 4 (b-d) show the spatial distribution of the elements C, O and Ce obtained from EDX in CeO2/CFP interlayer which are in accordance with the morphological information from the SEM image of Fig. 4a. This elemental mapping clearly indicates how the CeO₂ nanorods are uniformly anchored on the fibers of the carbon framework. The crystal structure of the commercial cellulose filter paper (FP), carbonized filter paper (CFP) and CeO₂/CFP membranes were characterized by X-ray diffraction (XRD) in the 2 θ angle range of 10 ° to 80 ° by putting the membranes on a zerobackground quartz sample holder. Fig. 4e shows that the filter paper presents the characteristic XRD peaks of Cellulose 1β (PDF # 00–060-1502). After carbonizing the cellulose paper at 800 $^{\circ}C$ for 2 h, the carbonized CFP shows broad XRD peaks at 24 $^{\circ}$ and 45 ° corresponding to (002) and (100) planes respectively from the graphitic carbon structure of CFP, which is a little bit shifted, but almost identical as previous reports [28,39]. After the hydrothermal growth of CeO₂ on CFP, the cubic phase CeO₂ is seen in the XRD pattern of the CeO₂/CFP sample which can be indexed to the cerium oxide PDF# 04-006-2393. These CeO₂ diffraction peaks were not seen in the CFP, indicating stable CeO2 crystals on the carbon framework. Raman spectroscopy was also employed to study more about the elemental coordination environment of the CFP and CeO₂/CFP membranes as shown in Fig. 4f. For the Raman spectrum of the CFP membrane, two peaks at approximately 1340 cm⁻¹ and 1590 cm⁻¹ were seen which correspond to the vibrational mode of the disordered carbon in the hybridized carbon ring (Dband) and symmetrical vibration bond of sp² bonded carbon atoms pair (G-band) respectively [28]. For the Raman spectra of CeO₂/CFP, the weak peaks the D and G bands from the carbon are evident, along with a strong peak at approximately 455 cm⁻¹ which corresponds to triply degenerate F_{2g} mode of CeO₂ fluorite structure [37,40]. The intensity ratio of the D and G bands (I_D/I_G) specifies

the negative correlation of the carbon graphitization degree [32]. The I_D/I_G ratio was recorded as 0.979 and 0.976 for the CFP and CeO₂/CFP film, respectively, indicating almost similar disorder in the sp² carbon lattice.

3.2. Cell electrochemical performance

To analyze the electrochemical behavior of CeO2/CFP as an interlayer in Li-S battery, 2032 type coin cells were assembled with commercial carbon cloth as cathode host material and lithium metal foil as anode. The sulfur was introduced by drop casting of lithium polysulfide catholyte on the carbon cloth. The CeO₂/CFP was sandwiched in between the carbon cloth and Celgard 2500 separator. The wide and open pore of pristine commercial carbon cloth cannot effectively trap the lithium polysulfides in the long term. Therefore, the 3D structure of carbon cloth, as cathode sulfur host material, was used as an ideal framework structure to effectively compare and evaluate the performance of the CeO₂/CFP interlayer in this study. The conventional electrolyte with LiTFSI salt in 1,3-dioxolane (DOL) and 1,2-dimethoxymethane (DME) with 1 wt% LiNO₃ additive was used in the cell assembling. The LiNO₃ additive was used to passivate the lithium to enhance Coulombic efficiency. All the assembled cells had 20 μL of the electrolyte. For 2 mg sulfur loading, 20 μL of 0.5 M Li₂S₆ catholyte was used. The whole battery assembling process was conducted in an argon filled glovebox under the condition of less than 0.1 ppm H₂O and less than 0.1 ppm O₂.

Fig. 5a shows the charge–discharge curve of the Li-S cell with CeO₂/CFP as interlayer at 0.2C current rate (1C = 1675 mA g⁻¹ of S) between 2.8 and 1.7 V versus Li⁺/Li. The two-plateau behavior during discharge and one plateau behavior during charge in the galvanostatic charge–discharge cycle are evident here just like the cyclic voltammetry curve of Fig. 6c. During discharge, the first plateau corresponds to the transformation of cyclo-octa S₈ to long chain soluble lithium polysulfides (Li₂S_n; 4 \leq n \leq 8) and the second plateau corresponds to the formation of short chain lithium polysulfides (Li₂S₂, Li₂S). The specific capacity calculation was based on the amount of sulfur in the cathode structure. For 2.0 mg S loading, the initial discharge capacity of the battery was recorded as 1177 mAhg⁻¹ at 0.2C and it was then stabilized around \sim 800 mAhg⁻¹ discharge capacity. The capacity contribution from the

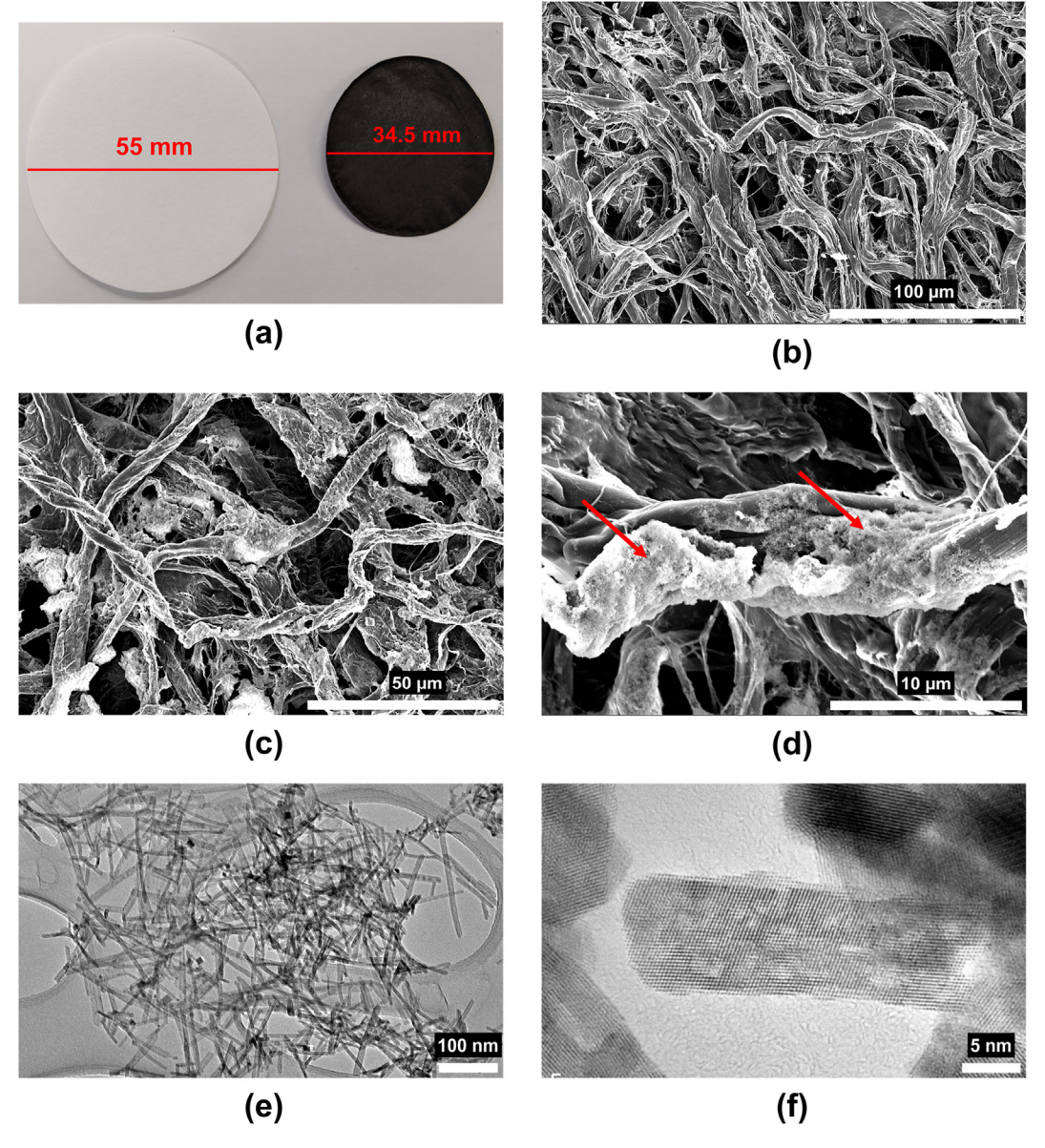


Fig. 3. a) Optical picture of the size comparison of pristine cellulose based filter paper (left) and carbon nanofiber film (right) after pyrolysis; b) SEM image of cross-linked carbon nanofibers derived from cellulose filter paper; c) SEM image of CeO₂ nanorods agglomerates homogeneously decorated on the cellulose derived carbon structure; d) Higher magnification image of a fiber decorated with CeO₂ nanorods. (e-f) TEM images of CeO₂ nanorods at various magnifications.

high plateau Q_H is about 625 mAhg⁻¹ which comes from the conversion of S_8 to $(Li_2S_x\colon x\ge 4)$ and from the low plateau region Q_L is about 552 mAhg⁻¹ which comes from the conversion of Li₂S₄ to final discharge products of Li₂S₂ and Li₂S. After 100 cycles, the specific capacity was recorded as 828 mAhg⁻¹, which was also stable even after 200 and 300 cycles at 804 and 775 mAhg⁻¹, respectively. This battery performance results demonstrate a significant improvement from the previously reported PPy/ZnO interlayer where the capacity at 0.2C degraded from 1194 mAhg⁻¹ to $\sim 600~\text{mAhg}^{-1}$ after 50 cycles with a capacity retention of only $\sim 50\%$ and a decay rate of 1% per cycle [41]. The fast capacity decay was due to the low conversion rate of sulfur containing species and uncontrollable growth of Li₂S after high polysulfide shuttling. Whereas, with full utilization of polysulfides by chemical and physical trapping and controllable growth of Li₂S, the CeO₂/CFP interlayer retained 65.8% of the initial discharge capacity after 300 cycles showing a capacity decay rate of only 0.11% per cycle, which further proves low capacity fading and enhanced electro-

chemical activity. In addition, if we consider the capacity after getting stabilized around $\sim 900 \; mAhg^{-1}$ after 10 cycles, the discharge capacity with cycle number curve in Fig. 5b is considerably flat, and the capacity retention can be measured as 83.1% with a decay rate of only 0.06% from cycle number 11 to 300. The long discharge plateaus of the curves indicate that the polysulfides generated in the discharge process were successfully trapped and adsorbed by the CeO₂/CFP interlayer, which reduced the dissolution of polysulfides in the electrolyte significantly. Even after 300 cycles, the long discharge plateau (Q_H) was observed as shown in Fig. 5a which further indicates fast polysulfide conversion after adsorption by CeO₂ nanorods, limiting dissolution of dissolved polysulfides. It is worth noting that the initial discharge capacity of the cell with CeO₂/CFP interlayer was slightly increased due to the activation process of the cell. This is due to the sulfur particles that are present in the electrochemically inactive sites become active after the other neighboring particles transform to lithium polysulfides. Then the large capacity loss after a few cycles was attributed to the insulat-

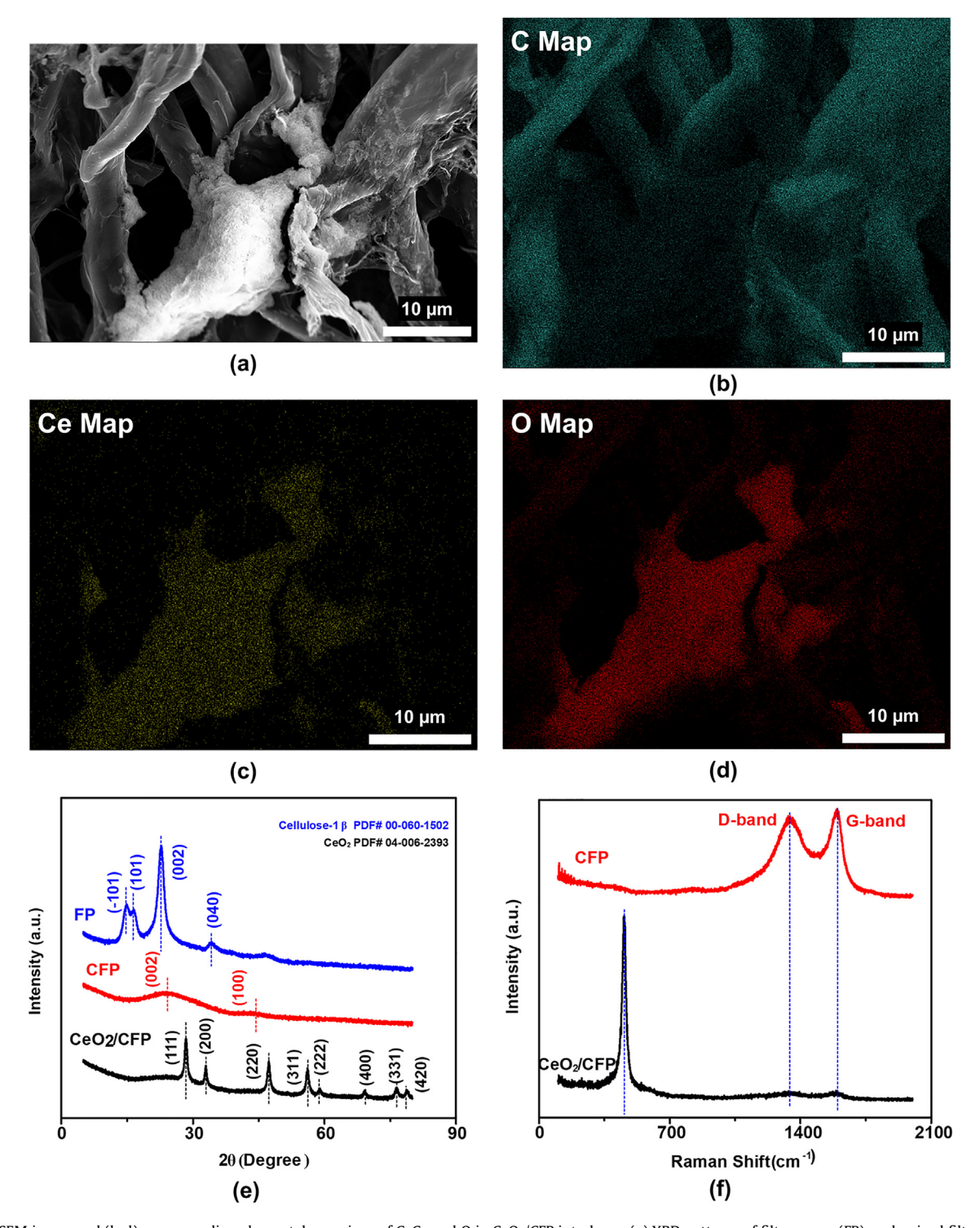


Fig. 4. (a) SEM image and (b-d) corresponding elemental mappings of C, Ce and O in CeO₂/CFP interlayer. (e) XRD patterns of filter paper (FP), carbonized filter paper (CFP) and CeO₂/CFP. (f) Raman spectra of CFP and CeO₂/CFP membrane.

ing nature of the formed Li_2S that covers some parts of the active CeO_2 .

Upon contact with the interlayer, lithium polysulfides got trapped in the CeO_2/CFP interlayer and then were further utilized in the cell. The cycling stability of the battery at 0.2C rate is also shown in the Fig. 5b. The battery was very stable at 0.2C for at least 300 cycles. Initially, the battery showed 1177 mAhg⁻¹, but after 3 cycles, it started to stabilize at around ~ 900 mAhg⁻¹. This high capacity at the initial cycles indicates that the CeO_2/CFP interlayer

successfully seizes the soluble lithium polysulfides during the first discharge. Even after 300 cycles, the battery retained specific capacity of about 775 mAhg⁻¹. This proves the effectiveness of the CeO₂/CFP interlayer that can trap the polysulfides and help retain the capacity of the battery. The Coulombic efficiency of the battery was maintained above 98% for all cycles except the 3rd cycle, which is further proof of interception of soluble lithium polysulfides and attenuation of shuttle effect. The low Coulombic efficiency in the initial cycles can be attributed to the formation of

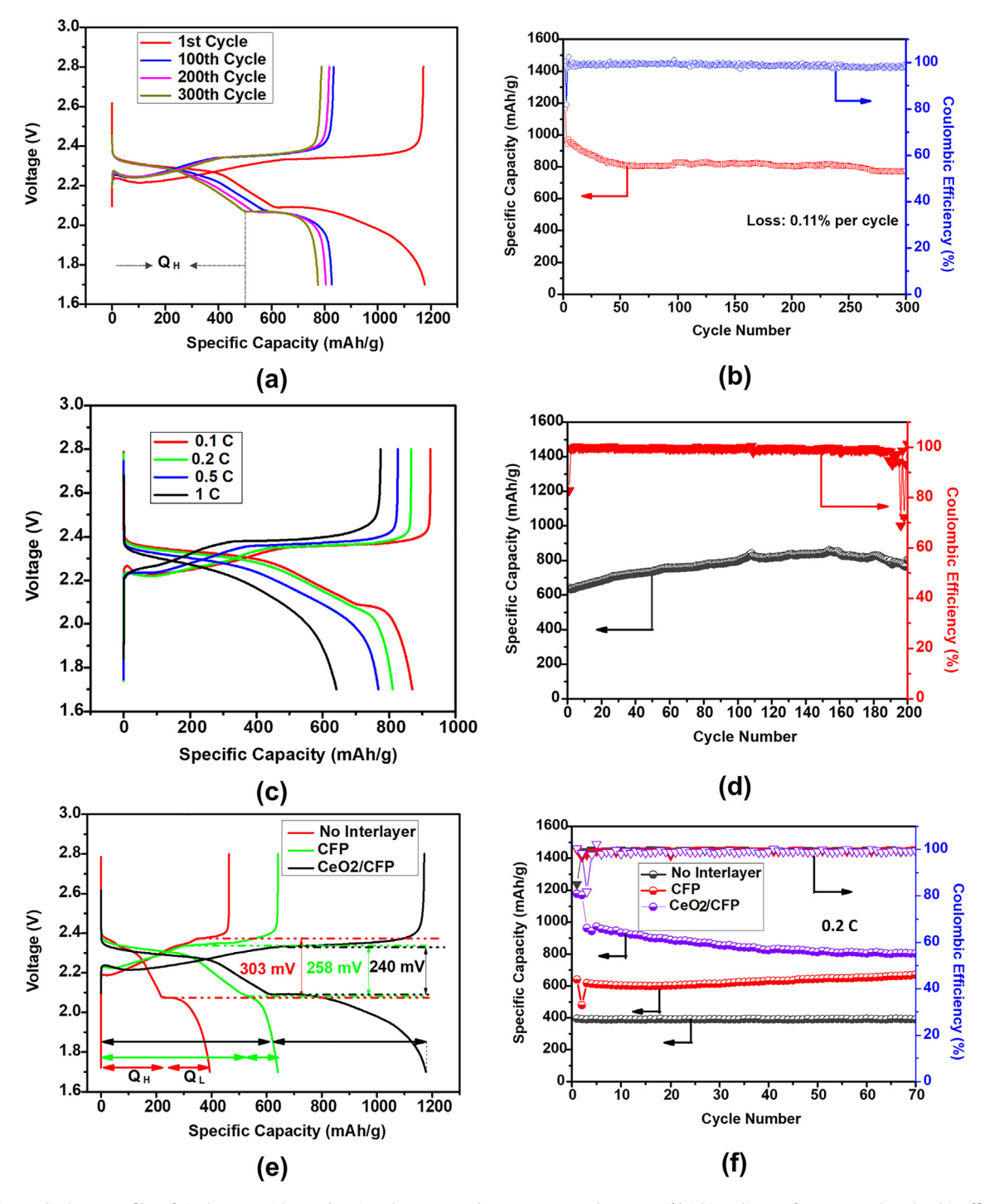


Fig. 5. a) Charge-discharge profiles of Li-S battery with CeO₂/CFP interlayer at 0.2C between 2.8 V and 1.7 V vs Li*/Li. b) Cycling performance and Coulombic efficiency at 0.2C for Li-S battery with CeO₂/CFP interlayer. c) Charge-discharge curve at various current densities for Li-S battery with CeO₂/CFP interlayer. d) Long term cycling performance of Li-S battery at 1C with CeO₂/CFP as interlayer. e) Li-S battery performance comparison at 0.2C for no interlayer, with CFP interlayer and CeO₂/CFP interlayer. f) Cycling performance and Coulombic efficiency.

Solid Electrolyte Interface (SEI) layer with excess Li ion utilization and electrolyte decomposition.

The robustness of the CeO₂/CFP interlayer can be evaluated by the rate performance of the battery by running it at different current densities. As shown in Fig. 5c, the cell with CeO₂/CFP interlayer shows reversible discharge capacities of 870 mAhg⁻¹, 810 mAhg⁻¹, 768 mAhg⁻¹ and 642 mAhg⁻¹ at 0.1C, 0.2C, 0.5C and 1C respectively, indicating an excellent rate capability. The 0.2C discharge capacity in Fig. 5c differs from Fig. 5a because, here, the bat-

tery was initially charged at slower current rate. Moreover, the Coulombic efficiency of these curves are less than 100% because these are the very first cycle at the respective current density. The Coulombic efficiency gradually stabilized to nearly 100% after a few cycles as the long cycling curves suggest. With the increasing current density, the discharge plateau gradually decreases due to the kinetic over voltage and polarization. Moreover, the reduced plateau could be the effect of the volume change of the electrolyte in the pore space because of the 80% volume expansion of S_8 to

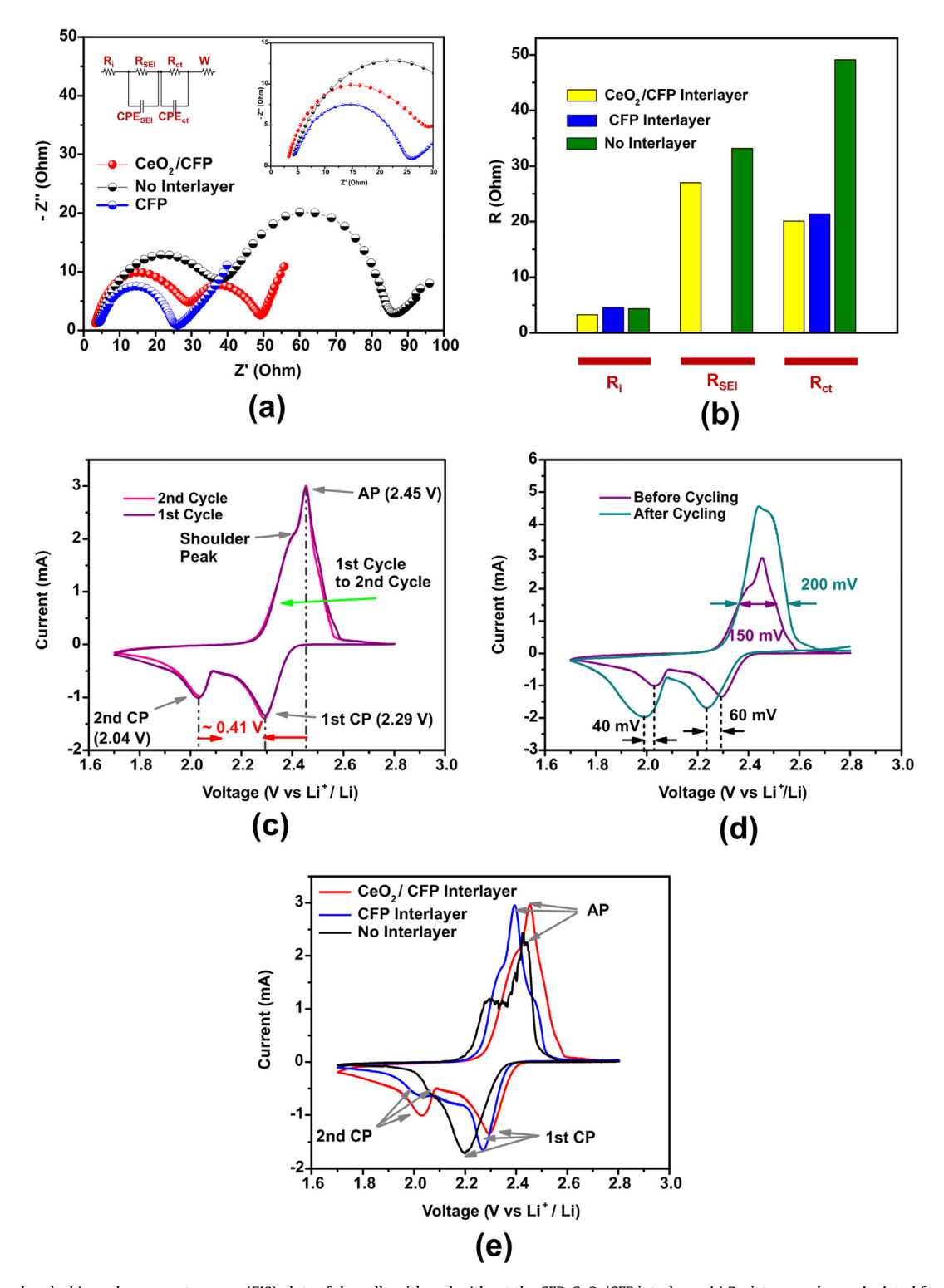


Fig. 6. a) Electrochemical impedance spectroscopy (EIS) plots of the cells with and without the CFP, CeO_2/CFP interlayer. b) Resistance values calculated from the EIS profiles with and without interlayer. c) Cyclic voltammogram (CV) of Li-S battery with the CeO_2/CFP interlayer at a potential sweep rate of 0.1 mV s⁻¹. d) CV comparison of the battery before and after 300 cycles at 0.2C. e) CV curves of Li-S battery without interlayer and with CFP and CeO_2/CFP interlayer at a scan rate of 0.1 mV s⁻¹.

Li₂S. Since the pores of the CFP interlayer are very small, the further decoration of CeO₂ makes the pores more confined. So, it experiences less electrolyte volume expansion that affects the second discharge plateau [42]. In comparison, the previously reported capacities for Li-S battery with Catecholamine-functionalized reduced graphene oxide cathode were 654 mAhg⁻¹ and 399 mAhg⁻¹ at 0.5C and 1C respectively, with the almost same sulfur

loading of 1 mg/cm² [43]. A stable discharge plateau was observed even at high current rate of 1C as shown in Fig. 5c. The outstanding electrochemical performance at different current densities manifests that the CeO₂/CFP interlayer can inhibit the shuttle effect of lithium polysulfides effectively and promote the cycling stability in the Li-S system. To further test the long-term stability of the cell with the CeO₂/CFP interlayer, the galvanostatic charge-discharge

cycles were tested at 1C for 100 cycles. Fig. 5d shows the long-term cycling performance and Coulombic efficiency of the Li-S battery with the CeO₂/CFP interlayer. The initial discharge capacity at 1C was recorded as 642 mAhg⁻¹ and it retained the specific capacity of 803 mAhg⁻¹ after 200 cycles. It is tremendous that even at high current density rating of 1C, after 200 cycles, the capacity of the battery didn't fall down, rather, it increased significantly by about 25.2%. This gradual increment in capacity could happen induced from the redistribution of active material in the sulfur cathode and due to the strong polysulfide adsorption efficiency of the CeO₂/CFP interlayer. The Coulombic efficiency was also maintained above 99% from the 2nd cycle except the final few cycles. The low Coulombic efficiency at the first cycle was due to the activation process of the sulfur electrode. This high Coulombic efficiency for long time indicates lacking corrosion of lithium anode. Overall, it demonstrates that the CeO₂/CFP interlayer leads to high discharge capacity at high current rate and maintains stable cyclability of the sulfur cathode. This significant enhancement in the electrochemical performance with improved capacity and cyclability even at high current rate of 1C is attributed to the encapsulation and restriction of lithium polysulfides migration by simultaneously physical and chemical binding effect of the CeO₂/CFP interlayer.

To provide in detail understanding of the effect of CeO₂ nanorods decorated carbonized filter paper as interlayer, a comparison of battery performance is given in the Fig. 5 e,f among three assembled Li-S batteries with no interlayer, with CFP or CeO₂/CFP as interlayer. Here, for all three types of batteries, a 1.5 cm² circular piece of carbon cloth was used as the cathode. The total sulfur loading was \sim 2 mg. Fig. 5e clearly shows that the initial discharge specific capacity for the battery without interlayer is a very low recording of 394 mAhg⁻¹ at 0.2C. This low specific capacity resulted from the lack of inhibition of polysulfides shuttling. Adding a CFP as interlayer improved the discharge capacity to 640 mAhg⁻¹. This improvement came from the physical entrapment of the polysulfides by the CFP interlayer. Decorating the CFP with CeO₂ nanorods further boosted the performance of the Li-S battery to 1177 mAhg⁻¹. This capacity increase of almost 198% than without interlayer further proves the effect of CeO₂ nanorods in retracting the polysulfides shuttling effect.

To evaluate the superiority of the CeO₂/CFP interlayer, the discharge capacity of the 3 types of cells were divided into high plateau (Q_H) and low plateau (Q_L) , as shown in Fig. 5e. The high plateau capacity of the cell with the CeO₂/CFP interlayer shows higher cycling stability compared with those of the cells with the CFP interlayer and no interlayer, which confirms the effective mitigation of higher order polysulfide (Li_2S_x : $x \ge 4$) dissolution due to the high adsorption capability of CeO₂ nanorods. The low plateau capacity (Q1), which corresponds to the conversion from Li2S4 to Li₂S₂/Li₂S, is also more stable for the cell with the CeO₂/CFP interlayer compared to the other two counterparts, indicating fast reaction kinetics in the conversion from lithium polysulfides to lithium sulfides. Therefore, it can be concluded that, the CeO₂/CFP interlayer can not only immobilize lithium polysulfides through physical and chemical interaction, but also provide enhanced conversion of lithium polysulfides and lithium sulfides. Moreover, the chargedischarge curve of the cell with the CeO2/CFP interlayer shows lower potential gap (Δ E) of 240 mV compared to the 303 mV and 258 mV values of the cell without interlayer and with the CFP interlayer respectively, demonstrating a significantly reduced polarization. This could be attributed to the high conductivity of carbon fiber and the catalytic effect of the surface engineered CeO₂ nanorods via Ce³⁺ and Ce⁴⁺ redox reaction and/or other surface defect reactions. Together with the dual mechanisms of physically and chemically entrapping the lithium polysulfides, the Li-S battery with the CeO₂/CFP interlayer shows superior performance than the other two batteries. The cycling performance data in

Fig. 5f also shows the superior rate performance of the cell with the CeO₂/CFP as interlayer compared to those of the cells with CFP only interlayer and no interlayer. The Coulombic efficiency was above 97% for all types of batteries. Even after 70 cycles, the specific capacity of the CeO₂/CFP interlayer battery was higher than the other two types of batteries. The specific capacity of the battery without interlayer remained lower because it has no mechanism to collect and reuse the soluble lithium polysulfides. The cycling stability of the cell with the CeO₂/CFP interlayer being less than its other counterparts could originate from the activation and/ or redistribution processes of the active materials in the cell. The sulfur particles at CeO₂ sites become electrochemically active by transforming neighboring sulfur to soluble lithium polysulfides. These polysulfides are trapped in the CeO₂/CFP interlayer and further utilized. The cell with no interlayer doesn't have this capability to collect and reuse the polysulfides, hence the stability is higher. The CFP has physical entrapment, so the stability is in between the cell with no interlayer and CeO₂/CFP interlayer.

Fig. S1 shows the cycling performance of Li-S battery with CeO_2/CFP interlayer with the sulfur content in cathode of 1.33 mg cm⁻² and 5.33 mg cm⁻² at 0.2C in terms of specific and areal capacity. Since sulfur is insulating material, increasing sulfur content in the cathode results in lower electronic conductivity. The batteries with the CeO_2/CFP interlayer with sulfur loadings of 1.33 mg cm⁻² and 5.33 mg cm⁻² provided high initial discharge capacity of 1177 mAh g⁻¹ (1.57 mAh cm⁻²) and 571 mAh g⁻¹ (3.04 mAh cm⁻²) respectively at 0.2C and the reversible discharge capacity after 150 cycles can be maintained at 827 mAh g⁻¹ (1.10 mAh cm⁻²) and 696 mAh g⁻¹ (3.71 mAh cm⁻²) respectively, indicating a high sulfur utilization when the CeO_2/CFP was used as interlayer. With a high sulfur content of 5.33 mg cm⁻², the rising trend of the discharge capacity may be originated from the redistribution of active material in the cathode. This excellent performance at high sulfur loading can be attributed to the use of the CeO_2/CFP interlayer with high conductivity and strong polysulfide confinement

These results are better or comparable to other reported CeO₂ based Li-S battery systems when important parameters like sulfur loading, electrolyte to sulfur ratio, cycling rate, number of cycles are considered. For example, Lu et al. reported specific capacity of 1033 mAhg⁻¹ and a reversible capacity of 723 mAhg⁻¹ after 100 cycles running at 0.2C rate ³³. Even with almost identical sulfur loading and higher electrolyte to sulfur ratio, their battery had higher capacity decay rate of 0.235% per cycle. Li et al. developed core shell structured CeO₂ inside porous carbon and reported specific capacity of 1242 mAhg⁻¹ which degraded to 663.3 mAhg⁻¹ after 100 cycles at 0.25C with a sulfur loading of approximately 0.7–1 mg/cm² [44]. A summary of the Li-S battery performance with other reported materials as cathode and interlayers is given in Table 1 to compare the results with the existing literatures.

3.3. Electrochemical impedance spectroscopy (EIS) and cyclic voltammetry (CV)

The electrochemical impedance spectroscopy (EIS) further outlines the role of the CeO_2/CFP interlayer in the Li-S battery by monitoring the internal resistance. Fig. 6a shows the Nyquist plot for the cell with CFP, CeO_2/CFP interlayer and without the interlayer within the frequency range from 100000 Hz to 0.1 Hz. The equivalent circuit is given in the inset figure. The X-intercept of the Nyquist curve in the high frequency region determines the combined ohmic resistance (R_i) of the cell. The first semicircle in the high frequency region is the resistance derived from the insulating solid electrolyte interface (SEI) layer denoted as R_{SEI} . The resistance due to the charge transfer process (R_{ct}) between the electrolyte and electrode interface is determined by the semicircles at the middle

Table 1Li-S battery performance summary and comparison with a few existing literatures.

Material	Sulfur loading mg/cm ²	Cycling rate	Number of cycles	Initial capacity (mAhg ⁻¹)	Reversible capacity (mAhg ⁻¹)	Capacity decay rate (% per cycle)	Ref.
CeO ₂ webbed CNT	1.3-1.6	0.2C	100	1033	723	0.235	[33]
S@CeO ₂ /PG	_	0.2C	_	1104	_	-	[45]
21	1.05	1C	500	710	348.6	0.068	
S/CeO ₂ /RGO	_	0.1C	200	1054	792	0.12	[36]
CeO ₂ /RGO *	2	0.1C	100	1136	886	0.24	[46]
S/CS-CeO ₂ /PC	0.7-1	0.25	100	1242.6	663.3	0.466	[44]
			500		421	0.015	
PPy/ZnO *	1.3	0.2C	50	1194	$\sim\!600$	1	[41]
VO ₂ /graphene	1.2	0.2C	200	1050	782	0.138	[47]
Activated carbon/ γ- MnO ₂	1	0.1C	100	926	541	0.41	[48]
Porous GO/CNT *	1	0.2C	100	1600	670	0.6	[49]
Co ₃ O ₄ @GC/N-CNT NF *	2	0.1C	250	1187	712	0.16	[50]
1 T-MoS ₂ / Carbon nanofiber *	1	0.1C	100	880	718	0.18	[51]
ZIF-7/CNF *	1.5	0.2C	100	1226.9	1091	0.11	[52]
CeO ₂ /GR-1.8 *	1	0.1C	350	1488	789.4	0.13	[53]
FS-SiO ₂ /C-CNFM *	1	0.1C	50	1304	934	0.57	[54]
MoS ₂ /G *	1.09	0.1C	300	1537.2	853.6	0.148	[55]
CeO ₂ /CFP	1.33	0.2C	300	1177	775	0.11	This work

^{*} Used as interlayer in Li-S battery

frequency region. This semicircle also represents reduction reaction kinetics in the sulfur cathode dominating the conversion from higher order lithium polysulfides (Li_2S_n : 4 < n < 8) to Li_2S_2/Li_2S . The inclined line in the lower frequency region represents the ion diffusion within the cathode (Warburg impedance). The cell with the CeO₂/CFP interlayer shows the impedance of only 3.25 Ohms (Table 2) which is lower than the ohmic resistance of the cell without interlayer. This reduction of impedance with the CeO₂/CFP interlayer is mainly due to the high conductivity of the carbon fiber matrix. As shown in Table 2, the R_{SEI} and R_{ct} (27.0 and 20.1 Ohms respectively) of the cell with the CeO₂/CFP interlayer are significantly lower than those (33.2 and 49.1 Ohms respectively) of the cell without interlayer. This mitigation of R_{SEI} after adding the interlayer means that the insulating SEI layer depletes after the interlayer insertion. The lower R_{ct} in the cell with the CeO₂/CFP interlayer proves that it improves the reaction kinetics of polysulfides conversion. The CFP interlayer consists of only one semicircle representing the charge transfer resistance R_{ct}. From the Nyquist curve, it is evident that the CFP interlayer improves the R_{ct} significantly than without interlayer. Unlike the cells without interlayer and with CeO₂/CFP interlayer, the CFP interlayer doesn't have the R_{SEI} semicircle because of highly conductive carbon fiber structure. The insulating CeO₂ NRs on the CFP could be the reason for the appearance of the R_{SEI} semicircle for the CeO₂/CFP interlayer. However, the lower R_{ct} of CeO₂/CFP interlayer compared to CFP proves the improvement of higher order to lower order polysulfide conversion during the electrochemical reaction. Fig. 6b shows a quantitative comparison of resistive parameters of the both type of cells. Specifically, the large difference in R_{ct} between the cells without and with the interlayer signifies fast polysulfide conversion reactions provided by the CeO₂/CFP interlayer. So, the overall electrochemical impedance shows that the CeO₂/CFP interlayer promotes the conversion of elemental sulfur to higher order soluble lithium polysulfides. The low impedance of the cell can also be

Table 2 EIS resistance analysis.

Cell	R _i (Ohms)	R _{SEI} (Ohms)	R _{ct} (Ohms)
Without Interlayer CFP Interlayer	4.3 4.54	33.2	49.1 21.42
CeO ₂ /CFP Interlayer	3.2	27.0	20.1

attributed to the good transportation of ions and high conductivity of the carbon framework in the interlayer that works as current collector as well. Moreover, CeO₂ nanorods can effectively reuse the dissolved active materials and provide enhanced performance by reducing surface aggregation. Table 2 shows the tabulated resistance parameters obtained from the EIS profiles.

The cyclic voltammetry (CV) measurement of the Li-S battery with the CeO2/CFP interlayer was conducted to gain an understanding of the redox reactions at a scan rate of 0.1 mVs⁻¹ with the potential range from 1.7 V to 2.8 V vs Li⁺/Li. As presented in Fig. 6c, the cell displays two obvious cathodic peaks at 2.29 V and 2.04 V and one anodic peak at 2.45 V which match very well with the typical charge-discharge profiles shown previously. These two cathodic peaks at 2.29 V and 2.04 V correspond to the reduction reactions from elemental cyclo-octa sulfur S₈ to soluble longchain lithium polysulfides (Li₂S_n; $4 \le n \le 8$) and then sequentially to insoluble short-chain lithium polysulfides (Li₂S₂, Li₂S) respectively. The anodic peak corresponds to the reverse process. Furthermore, the CV profile presents sharp and high chargedischarge peaks which verify the rapid electron and/or ion transfer processes. The almost overlapping curves for the first two CV cycles with no severe potential shifts also indicate the high polysulfides trapping ability and cycling stability of the CeO2/CFP interlayer-based cell. The large current densities of the cathodic and anodic peaks demonstrate high conductivity and fast reaction kinetics which successively enhances the specific capacity and rate cycling capability. Fig. 6d shows the CV curves for the cell before and after cycling at 0.2C for 300 cycles. Even after 300 cycles, the CV curves maintain the characteristic redox peaks which shifted a little and became much broader. This indicates the excellent reversibility and cyclability of the battery cell. Fig. 6e shows the comparison CV profiles of the cells without interlayer and with CFP, CeO₂/CFP interlayer. The 2nd cathodic peak of the cell with the CeO₂/CFP interlayer is stronger than the same peaks of the other two cells. For the cell without interlayer, this cathodic peak is very weak, demonstrating no polysulfide blocking and conversion. The 2nd anodic peak of the cell with CFP interlayer is a little larger and provides some sort of polysulfide inhibition. Since this 2nd anodic peak signifies the conversion of soluble long-chain lithium polysulfides (Li₂S_n; $4 \le n \le 8$) and to insoluble shortchain lithium polysulfides (Li₂S₂, Li₂S), the stronger peak of the cell

with the CeO₂/CFP interlayer provides another evidence of excellent polysulfide blocking and fast polysulfide conversion.

3.4. Microstructure analysis after cycling

To further understand the detailed polysulfides adsorption mechanism, the Li-S battery cells were disassembled inside an argon filled glovebox after 300 cycles at 0.2C. The integrity microstructure of the CeO₂/CFP interlayer was well maintained as shown in the SEM images of Fig. 7(a-b). No cracks were observed on the cycled CeO₂/CFP interlayer which indicates that the CeO2 nanorods can effectively entrap the polysulfides within the interlayer structure. As a result, the capacity decay in the battery was retarded during the cycling. The open pores of the carbon nanofibers were also maintained for fast lithium ion migration. However, after cycling, the initially smooth surface of lithium foil became rough as shown in Fig. 7c. As reported previously, it could be protected using different methods to enhance the performance of the Li-S battery [18,56]. The high Coulombic efficiency of the battery also stems from the fact that the interlayer successfully inhibited the reaction between the polysulfides and lithium foil. The focus of this study was on the interlayer, so the lithium corrosion, dendrite formation, electrolyte decomposition and depletion issues were overlooked which can be the cause of capacity fading as well. However, the Li₂S deposition on the surface of the lithium foil were not seen for the samples with interlayer, which is attributed to the polysulfide interception by the CeO₂/CFP interlayer. The visual inspection of the condition of the separators can be seen in the optical images of Fig. 7d. The separator from the disassembled cell with the CeO₂/CFP interlayer (the bottom picture of Fig. 7d) was fresh and clean with no obvious yellow colored polysulfide in it, indicating immobilization of polysulfides by the CeO_2/CFP interlayer. Whereas, the separator from the cycled cell without interlayer (the top picture of Fig. 7**d**) was yellow colored representing poor restriction of polysulfide diffusion.

To confirm the lithium polysulfide trapping in the CeO₂/CFP interlayer, EDS elemental mapping was conducted on the cycled interlayer sample. From Fig. 8(a-b), it is clearly seen that the sulfur was trapped effectively and homogeneously distributed on the carbon fiber structure, confirming polysulfides adsorption by the CeO₂/CFP interlayer. This occurrence happens because the CeO₂ nanorods attached on the carbon fiber framework and chemically bound the polysulfides on the surface of the interlayer, promoting polysulfide redox kinetics and cell efficiency. To validate the chemical binding effect of the CeO₂/CFP layer with lithium polysulfides, 20 mg of CeO₂/CFP powder was first added in 0.5 mL of 5 mM Li₂S₆ catholyte. After keeping it overnight, the excess catholyte was dumped and the powder was dried at 60 °C overnight in a vacuum oven. The XPS analysis was then conducted to investigate the chemical interaction between the interlayer and lithium polysulfides. The S 2p spectra in Fig. 8c show two S $2p_{3/2}$ contributions at 164.1 and 162.6 eV which represent the bridging (S_B^0) and terminal (S_T^{-1}) sulfur. The peak at 169.2 eV corresponds to polythionate complex. As mentioned by Nazar et al. [57], this polythionate complex can accelerate the polysulfide conversion and result in fast electrocatalytic activity. The u and v peaks representing the spin orbit splitting of Ce $3d_{5/2}$ and Ce $3d_{3/2}$ are shown in Fig. 8d [37,58]. These u"/v", u""/v" pairs of peaks are originated from various Ce 4f electron configuration of Ce⁴⁺ species. The u'/v' peaks are

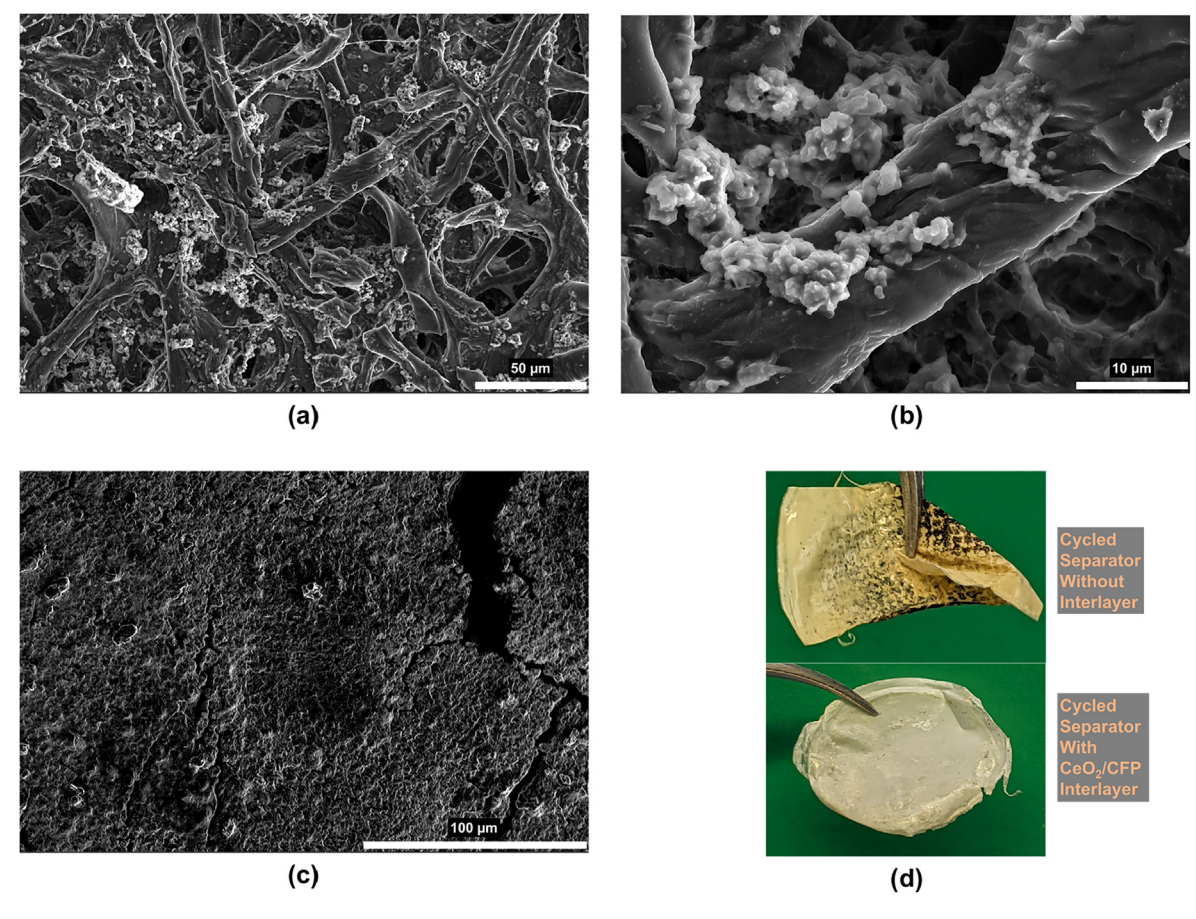
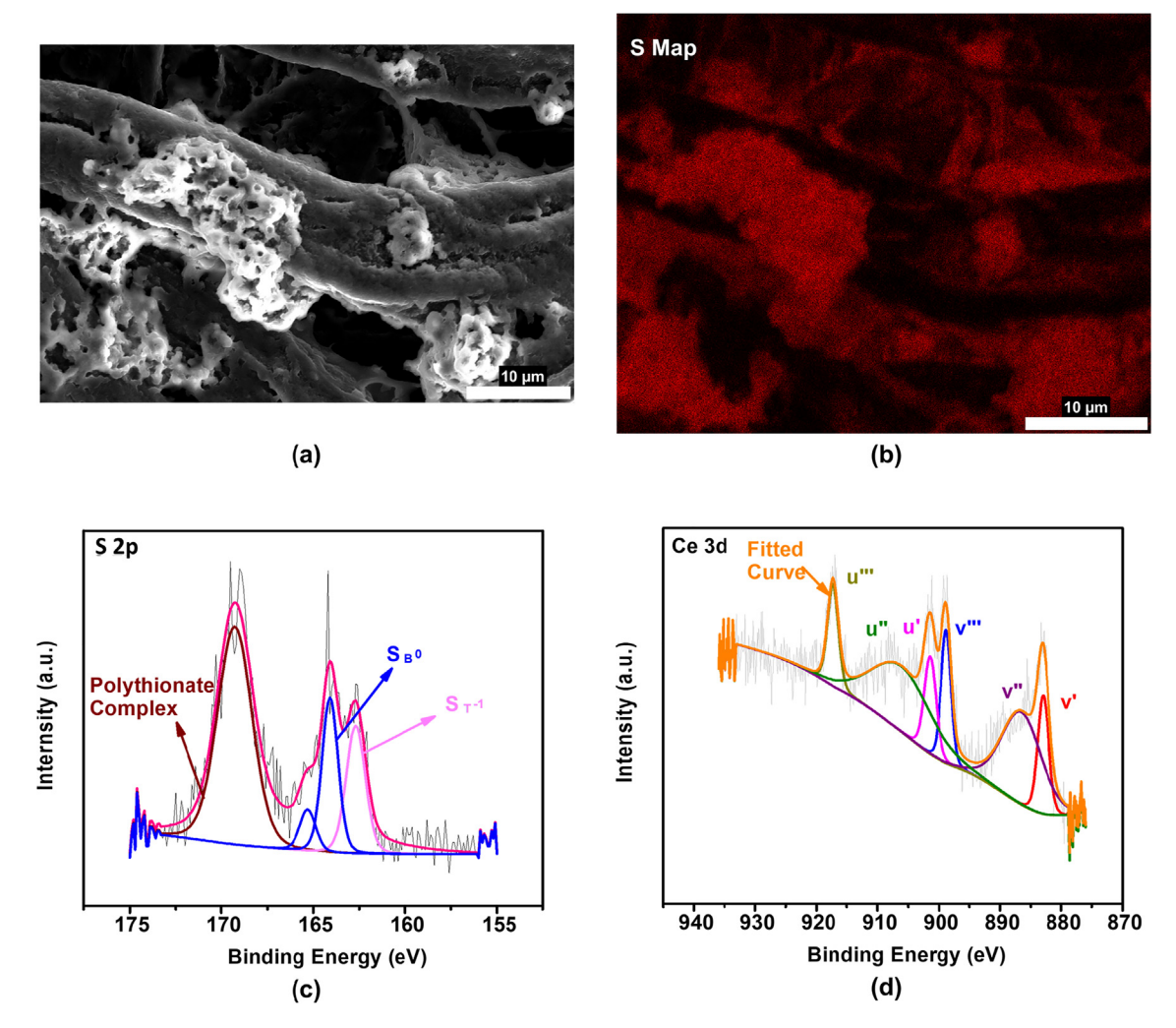


Fig. 7. SEM images of (a-b) CeO₂/CFP interlayer and c) lithium foil after 300 cycles at 0.2C rate. d) Optical images of separators from the disassembled batteries with and without CeO₂/CFP interlayer.



 $\textbf{Fig. 8.} \ a) \ \text{SEM image of the cycled CeO}_2/\text{CFP interlayer; b)} \ Elemental \ mapping \ of \ S; \ c) \ S \ 2p \ and \ d) \ Ce \ 3d \ XPS \ spectra \ of \ Li_2S_6/\text{CeO}_2/\text{CFP}.$

induced from the two electron configuration of Ce^{3+} species [37,59].

In order to visually examine and compare the polysulfide trapping proficiency of CeO $_2$ /CFP, a visual discrimination adsorption test was performed. The CFP and CeO $_2$ /CFP films of 20 mg each were mechanically grinded into powders in a mortar and were dispersed in 0.5 mL of 5 mM Li $_2$ S $_6$ in DOL/DME (volume ratio 1:1) solution. The color variation of the solutions was compared with blank catholyte after aging for different times (0 h, 4 h, 8 h, and 12 h) as shown in Fig. 9. Compared to the blank solution and the solution containing CFP, the solution containing CeO $_2$ /CFP became transparent gradually in 12 h. This demonstrates that CeO $_2$ /CFP shows strong absorption towards Li $_2$ S $_6$ compared to CFP. Therefore, CeO $_2$ /CFP is more capable of suppressing the lithium polysulfide diffusion and improving sulfur utilization.

4. Conclusion

An environmentally friendly and cost-effective method to fabricate potent cathode interlayer for Li-S battery, based on CeO_2 nanorods decorated on cellulose paper derived carbon fiber framework, has been demonstrated to alleviate the polysulfide shuttle effect. Li-S battery with this interlayer demonstrated a high discharge capacity of 1177 mAhg $^{-1}$ and efficiency of more than 98% at 0.2C current rate with high cycling stability. Even at 1C rate, the battery delivered a specific capacity of 803 mAhg $^{-1}$ after 200

cycles. The proposed interlayer was shown to be very effective to mitigate polysulfides shuttling and self-discharging problem of the Li-S battery. The high capacity retention and the cycling stability at different current rates indicate that such design of CeO₂/CFP interlayer as "vice-electrode" is a highly feasible approach towards commercialization of Li-S battery. The adsorption and reutilization of the dissolved polysulfides by CeO₂ nanorods and the high conductivity of the carbon fiber network are the primary reasons for the improved performance of the battery. Our data suggests that it can be an easy yet economical method to design practical Li-S battery for future energy storage applications.

CRediT authorship contribution statement

Sakibul Azam: Investigation, Methodology, Formal analysis, Writing – original draft, Writing – review & editing. **Zhen Wei:** Investigation, Writing – review & editing. **Ruigang Wang:** Conceptualization, Investigation, Methodology, Supervision, Formal analysis, Writing – review & editing, Funding acquisition.

Declaration of Competing Interest

The authors declare that they have no known competing financial interests or personal relationships that could have appeared to influence the work reported in this paper.

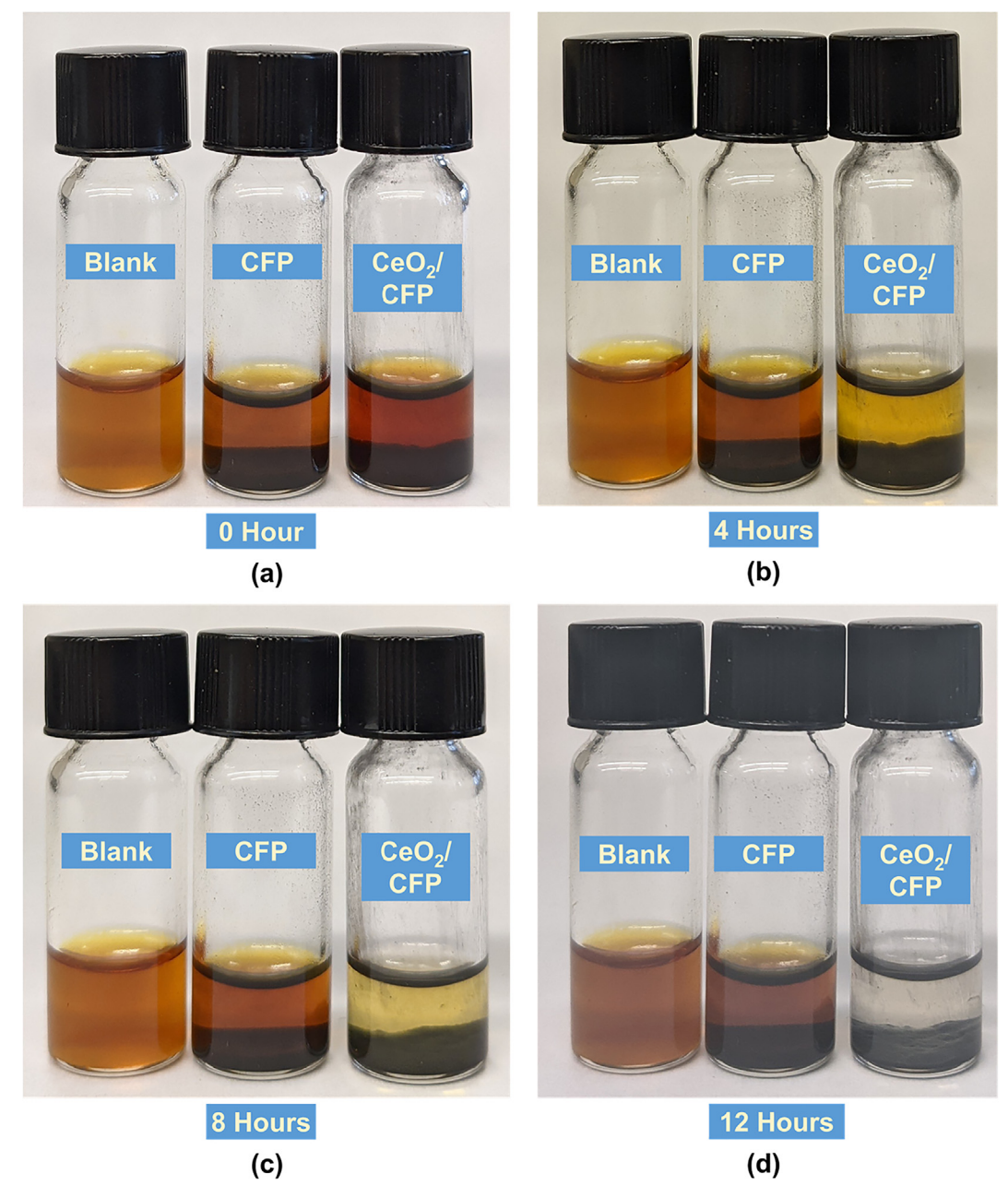


Fig. 9. Visual polysulfide adsorption experiments for different times (0 h, 4 h, 8 h, and 12 h): digital images of blank 5 mM Li_2S_6 catholyte (left), 20 mg of CFP powder (middle) and CeO_2/CFP powder (right) in 5 mM Li_2S_6 .

Acknowledgement

This work is supported by the National Science Foundation (CBET-2118784 and IIP-2147564). This project also receives partial financial support from Alabama Transportation Institute. The use of electron microscopy facilities at the Alabama Analytical Research Center (AARC), The University of Alabama, is gratefully acknowledged.

Appendix A. Supplementary material

Supplementary data to this article can be found online at https://doi.org/10.1016/j.jcis.2022.01.161.

References

- [1] P.G. Bruce, S.A. Freunberger, L.J. Hardwick, J.-M. Tarascon, Li-O₂ and Li-S batteries with high energy storage, Nat. Mater. 11 (1) (2012) 19.
- [2] A.R. Armstrong, P.G. Bruce, Synthesis of layered LiMnO₂ as an electrode for rechargeable lithium batteries, Nature 381 (6582) (1996) 499–500.
- [3] Z. Chen, J. Dahn, Methods to obtain excellent capacity retention in LiCoO₂ cycled to 4.5 V, Electrochimica Acta 49 (7) (2004) 1079–1090.
- [4] H. Huang, S.-C. Yin, L.S. Nazar, Approaching theoretical capacity of LiFePO₂ at room temperature at high rates, Electrochemical and Solid State Letters 4 (10) (2001) A170.
- [5] B. Kang, G. Ceder, Battery materials for ultrafast charging and discharging, Nature 458 (7235) (2009) 190–193.
- [6] K. Kang, Y.S. Meng, J. Breger, C.P. Grey, G. Ceder, Electrodes with high power and high capacity for rechargeable lithium batteries, Science 311 (5763) (2006) 977–980.
- [7] J. Tarascon, E. Wang, F. Shokoohi, W. McKinnon, S. Colson, The spinel phase of LiMn₂O₄ as a cathode in secondary lithium cells, J. Electrochem. Soc. 138 (10) (1991) 2859.

- [8] K. Tatsumi, Nano Aspects of Advanced Positive Electrodes for Lithium-Ion Batteries, Springer, In Nanoscale Technology for Advanced Lithium Batteries, 2014, pp. 23–30.
- [9] Y. Xia, Y. Zhou, M. Yoshio, Capacity fading on cycling of 4 V Li/LiMn₂O₄ Cells, J. Electrochem. Soc. 144 (8) (1997) 2593.
- [10] B.H. Jeon, J.H. Yeon, K.M. Kim, I.J. Chung, Preparation and electrochemical properties of lithium–sulfur polymer batteries, J. Power Sources 109 (1) (2002) 89–97.
- [11] D. Marmorstein, T. Yu, K. Striebel, F. McLarnon, J. Hou, E. Cairns, Electrochemical performance of lithium/sulfur cells with three different polymer electrolytes, J. Power Sources 89 (2) (2000) 219–226.
- [12] J. Shim, K.A. Striebel, E.J. Cairns, The lithium/sulfur rechargeable cell: effects of electrode composition and solvent on cell performance, J. Electrochem. Soc. 149 (10) (2002) A1321.
- [13] Y. Diao, K. Xie, S. Xiong, X. Hong, Shuttle phenomenon–The irreversible oxidation mechanism of sulfur active material in Li–S battery, J. Power Sources 235 (2013) 181–186.
- [14] Y.V. Mikhaylik, J.R. Akridge, Polysulfide shuttle study in the Li/S battery system, J. Electrochem. Soc. 151 (11) (2004) A1969.
- [15] J. Xiao, J.Z. Hu, H. Chen, M. Vijayakumar, J. Zheng, H. Pan, E.D. Walter, M. Hu, X. Deng, J. Feng, Following the transient reactions in lithium-sulfur batteries using an in situ nuclear magnetic resonance technique, Nano Lett. 15 (5) (2015) 3309–3316.
- [16] S.S. Zhang, Liquid electrolyte lithium/sulfur battery: fundamental chemistry, problems, and solutions, J. Power Sources 231 (2013) 153–162.
- [17] M. Shaibani, M.S. Mirshekarloo, R. Singh, C.D. Easton, M.D. Cooray, N. Eshraghi, T. Abendroth, S. Dörfler, H. Althues, S. Kaskel, Expansion-tolerant architectures for stable cycling of ultrahigh-loading sulfur cathodes in lithium-sulfur batteries, Sci. Adv. 6 (1) (2020) eaay2757.
- [18] X. Xu, S. Wang, H. Wang, B. Xu, C. Hu, Y. Jin, J. Liu, H. Yan, The suppression of lithium dendrite growth in lithium sulfur batteries: a review, J. Storage Mater. 13 (2017) 387–400.
- [19] A. Jozwiuk, B.B. Berkes, T. Weiß, H. Sommer, J. Janek, T. Brezesinski, The critical role of lithium nitrate in the gas evolution of lithium–sulfur batteries, Energy Environ. Sci. 9 (8) (2016) 2603–2608.
- [20] X. Gao, Y. Huang, Z. Guang, X. Li, Constructing a Multifunctional Globular Polypyrrole Slurry Cladding Carbon Aerogel/Sulfur Cathode for High-Performance Lithium-Sulfur Batteries, Energy Fuels 34 (3) (2020) 3931–3940.
- [21] X. Gao, Y. Huang, X. Li, H. Gao, T. Li, SnP0.94 nanodots confined carbon aerogel with porous hollow superstructures as an exceptional polysulfide electrocatalyst and "adsorption nest" to enable enhanced lithium-sulfur batteries, Chem. Eng. J. 420 (2021).
- [22] X. Gao, Y. Huang, Z. Zhang, S. Batool, X. Li, T. Li, Porous Hollow Carbon Aerogel-Assembled Core@Polypyrrole Nanoparticle Shell as an Efficient Sulfur Host through a Tunable Molecular Self-Assembly Method for Rechargeable Lithium/Sulfur Batteries, ACS Sustainable Chem. Eng. 8 (42) (2020) 15822–15833.
- [23] Y. Huang, X. Gao, X. Han, Z. Guang, X. Li, Controlled synthesis of three-dimensional porous carbon aerogel via catalysts: effects of morphologies toward the performance of lithium-sulfur batteries, Solid State Ionics 347 (2020).
- [24] C. Ma, Z. Zheng, X. Jia, X. Liu, J. Wang, W. Qiao, L. Ling, Promoting the synergistic effect of sulfur immobilization and polysulfides trapping by nitrogen functionalized interconnected hollow carbon nanocages for highperformance lithium-sulfur batteries, J. Power Sources 486 (2021).
- [25] Y.-S. Su, A. Manthiram, A new approach to improve cycle performance of rechargeable lithium-sulfur batteries by inserting a free-standing MWCNT interlayer, Chem. Commun. 48 (70) (2012) 8817–8819.
- [26] Y.-S. Su, A. Manthiram, Lithium-sulphur batteries with a microporous carbon paper as a bifunctional interlayer, Nat. Commun. 3 (1) (2012) 1–6.
- [27] L. Fan, M. Li, X. Li, W. Xiao, Z. Chen, J. Lu, Interlayer Material Selection for Lithium-Sulfur Batteries, Joule 3 (2) (2019) 361–386.
- [28] S. Li, G. Ren, M.N.F. Hoque, Z. Dong, J. Warzywoda, Z. Fan, Carbonized cellulose paper as an effective interlayer in lithium-sulfur batteries, Appl. Surf. Sci. 396 (2017) 637–643.
- [29] Y. Huang, M. Zheng, Z. Lin, B. Zhao, S. Zhang, J. Yang, C. Zhu, H. Zhang, D. Sun, Y. Shi, Flexible cathodes and multifunctional interlayers based on carbonized bacterial cellulose for high-performance lithium-sulfur batteries, J. Mater. Chem. A 3 (20) (2015) 10910–10918.
- [30] Z.W. Seh, J.H. Yu, W. Li, P.-C. Hsu, H. Wang, Y. Sun, H. Yao, Q. Zhang, Y. Cui, Two-dimensional layered transition metal disulphides for effective encapsulation of high-capacity lithium sulphide cathodes, Nat. Commun. 5 (1) (2014) 1–8.
- [31] S.-I. Oh, J.-C. Kim, D.-W. Kim, Cellulose-derived tin-oxide-nanoparticleembedded carbon fibers as binder-free flexible Li-ion battery anodes, Cellulose 26 (4) (2019) 2557–2571.
- [32] H. Wang, B. Zhang, X. Zeng, L. Yan, J. Zheng, M. Ling, Y. Hou, Y. Lu, C. Liang, 3D porous carbon nanofibers with CeO2-decorated as cathode matrix for high performance lithium-sulfur batteries, J. Power Sources 473 (2020).
- [33] D. Xiao, C. Lu, C. Chen, S. Yuan, CeO₂-webbed carbon nanotubes as a highly efficient sulfur host for lithium-sulfur batteries, Energy Storage Mater. 10 (2018) 216–222.

- [34] X. Qian, L. Jin, L. Zhu, S. Yao, D. Rao, X. Shen, X. Xi, K. Xiao, S. Qin, CeO₂ nanodots decorated ketjen black for high performance lithium–sulfur batteries, RSC Adv. 6 (112) (2016) 111190–111196.
- [35] L. Ma, R. Chen, G. Zhu, Y. Hu, Y. Wang, T. Chen, J. Liu, Z. Jin, Cerium Oxide Nanocrystal Embedded Bimodal Micromesoporous Nitrogen-Rich Carbon Nanospheres as Effective Sulfur Host for Lithium-Sulfur Batteries, ACS Nano 11 (7) (2017) 7274–7283.
- [36] Q. Hao, G. Cui, Y. Tian, T. Tan, Y. Zhang, Three-Dimensional S/CeO₂/RGO Composites as Cathode Materials for Lithium-Sulfur Batteries, Materials (Basel) 11 (9) (2018).
- [37] Z. Wei, J. Li, Y. Wang, R. Wang, High-performance Li-S batteries enabled by polysulfide-infiltrated free-standing 3D carbon cloth with CeO₂ nanorods decoration, Electrochimica Acta 388 (2021).
- [38] M. Hagen, D. Hanselmann, K. Ahlbrecht, R. Maça, D. Gerber, J. Tübke, Lithium-Sulfur Cells: the Gap between the State-of-the-Art and the Requirements for High Energy Battery Cells, Adv. Energy Mater. 5 (16) (2015).
- [39] X. Ma, C. Yuan, X. Liu, Mechanical, Microstructure and Surface Characterizations of Carbon Fibers Prepared from Cellulose after Liquefying and Curing, Materials (Basel) 7 (1) (2013) 75–84.
- [40] Z. Liu, J. Li, M. Buettner, R.V. Ranganathan, M. Uddi, R. Wang, Metal-Support Interactions in CeO₂- and SiO₂-Supported Cobalt Catalysts: effect of Support Morphology, Reducibility, and Interfacial Configuration, ACS Appl Mater Interfaces 11 (18) (2019) 17035–17049.
- [41] F. Yin, J. Ren, Y. Zhang, T. Tan, Z. Chen, A PPy/ZnO functional interlayer to enhance electrochemical performance of lithium/sulfur batteries, Nanoscale Res Lett 13 (1) (2018) 307.
- [42] P. Barai, A. Mistry, P.P. Mukherjee, Poromechanical effect in the lithium–sulfur battery cathode, Extreme Mech. Lett. 9 (2016) 359–370.
- [43] S.A. Ahad, P.R. Kumar, J.-H. Kim, D.J. Kim, P. Ragupathy, D.K. Kim, Catecholamine-Functionalized Reduced Graphene Oxide: a Scalable Carbon Host for Stable Cycling in Lithium-Sulfur Batteries, Electrochimica Acta 246 (2017) 451–458.
- [44] X. Chén, L. Li, Y. Shan, D. Zhou, W. Cui, Y. Zhao, Synergistic effect of cerium oxide with core-shell structure embedded in porous carbon for highperformance lithium-sulfur batteries. *Materials Today*, Communications 27 (2021)
- [45] M. Kim, J. Lee, Y. Jeon, Y. Piao, Phosphorus-doped graphene nanosheets anchored with cerium oxide nanocrystals as effective sulfur hosts for high performance lithium-sulfur batteries, Nanoscale 11 (29) (2019) 13758–13766.
- [46] S. Wang, F. Gao, Y. Zhao, N. Liu, T. Tan, X. Wang, Two-Dimensional CeO₂/RGO Composite-Modified Separator for Lithium/Sulfur Batteries, Nanoscale Res Lett 13 (1) (2018) 377.
- [47] Y. Ning, B. Wang, F. Jin, J. Yang, J. Zhang, H. Luo, F. Wu, Z. Zhang, H. Zhang, Y. Zhou, D. Wang, A rational VO₂ nanotube/graphene binary sulfur host for superior lithium-sulfur batteries, J. Alloy. Compd. 838 (2020).
- [48] F. Luna-Lama, C. Hernández-Rentero, A. Caballero, J. Morales, Biomass-derived carbon/γ-MnO₂ nanorods/S composites prepared by facile procedures with improved performance for Li/S batteries, Electrochimica Acta 292 (2018) 522– 531.
- [49] J.-Q. Huang, Z.-L. Xu, S. Abouali, M. Akbari Garakani, J.-K. Kim, Porous graphene oxide/carbon nanotube hybrid films as interlayer for lithium-sulfur batteries, Carbon 99 (2016) 624–632.
- [50] R. Saroha, J.H. Oh, J.S. Lee, Y.C. Kang, S.M. Jeong, D.-W. Kang, C. Cho, J.S. Cho, Hierarchically porous nanofibers comprising multiple core-shell Co₃O₄@graphitic carbon nanoparticles grafted within N-doped CNTs as functional interlayers for excellent Li–S batteries, Chem. Eng. J. 426 (2021).
- [51] S.-H. Moon, M.-C. Kim, J.-H. Choi, Y.-S. Kim, H. Kim, K.-W. Park, 1T-MoS₂/carbon nanofiber composite as an interlayer fabricated by an in situ electrochemical fabrication method for lithium-sulfur batteries, J. Alloy. Compd. 857 (2021).
- [52] S. Zheng, D. Sun, L. Wu, S. Liu, G. Liu, Carbon fiber supported two-dimensional ZIF-7 interlayer for durable lithium-sulfur battery, J. Alloy. Compd. 870 (2021).
- [53] F. Zhu, M. Zhang, X. Cao, CeO₂/GR interlayer prepared to reinforce the cathode and promote the electrochemical performance of lithium-sulfur batteries, Synth. Met. 282 (2021).
- [54] A. Belgibayeva, I. Taniguchi, Insights into the improved electrochemical performance of lithium–sulfur battery with free-standing SiO₂/C composite nanofiber mat interlayer, J. Power Sources 484 (2021).
- [55] X. Fang, M. Zhang, MoS₂/G interlayer as a polysulfide immobilization apparatus for high-performance lithium-sulfur batteries, Ionics 27 (9) (2021) 3875–3885.
- [56] Y. Luo, L. Guo, M. Xiao, S. Wang, S. Ren, D. Han, Y. Meng, Strategies for inhibiting anode dendrite growth in lithium-sulfur batteries, J. Mater. Chem. A 8 (9) (2020) 4629–4646.
- [57] X. Liang, C. Hart, Q. Pang, A. Garsuch, T. Weiss, L.F. Nazar, A highly efficient polysulfide mediator for lithium-sulfur batteries, Nat Commun 6 (2015) 5682.
- [58] Y. Peng, C. Wang, J. Li, Structure–activity relationship of VOx/CeO₂ nanorod for NO removal with ammonia, Appl. Catal. B 144 (2014) 538–546.
- [59] W. Qi, W. Jiang, F. Xu, J. Jia, C. Yang, B. Cao, Improving confinement and redox kinetics of polysufides through hollow NC@CeO₂ nanospheres for highperformance lithium-sulfur batteries, Chem. Eng. J. 382 (2020).